EES Batteries

PAPER

View Article Online
View Journal

Cite this: DOI: 10.1039/d5eb00131e

Spatially heterogeneous degradation in $LiFePO_4$// graphite pouch batteries under temperature accelerated aging process

Jialong Zhou,[a,b] Jinyang Dong,*[a,b] Yun Lu,[a,b] Kang Yan,[b] Yibiao Guan,*[c] Fangze Zhao,[d] Rui Tang,[a,b] Wenjun Shen,[a,b] Ning Li,[a,b] Yuefeng Su,*[a,b] Feng Wu[a,b] and Lai Chen *[a,b]

The accelerated degradation of lithium-ion batteries under elevated temperature has emerged as a critical challenge for large-format energy storage systems. While thermal stress is known to intensify performance decline, its spatial influence within individual batteries remains underexplored. This study investigates the position-dependent aging behavior of $LiFePO_4$//graphite (LFP//Gr) pouch batteries subjected to long-term cycling at 25 °C and 45 °C. A spatially resolved, multi-scale analysis framework is employed to differentiate degradation characteristics between inner and outer electrode regions. The results reveal that temperature-accelerated aging leads to pronounced spatial heterogeneity in electrochemical performance, structural evolution, and interfacial stability, with inner regions showing more severe deterioration. Irreversible lithium inventory loss emerges as the dominant degradation mechanism, primarily driven by intensified interfacial reactions and uneven side-product accumulation. These findings demonstrate that battery aging under high-temperature conditions is not spatially uniform and that internal position significantly influences degradation severity. The study highlights the limitations of homogeneous evaluation methods and underscores that spatial heterogeneity must be explicitly considered when analyzing and modeling temperature-accelerated aging processes. This work provides mechanistic insight essential for developing thermally robust and spatially optimized lithium-ion batteries for demanding applications such as electric vehicles and stationary energy storage.

Received 16th July 2025,
Accepted 31st July 2025

DOI: 10.1039/d5eb00131e

rsc.li/EESBatteries

Broader context

Evaluating temperature-accelerated aging is essential for improving the durability and safety of lithium-ion batteries used in electric vehicles and energy storage systems. This study explores how elevated temperatures drive spatially heterogeneous degradation in $LiFePO_4$//graphite pouch cells, with a focus on differences between inner and outer electrode regions. The results demonstrate that thermal stress induces distinct degradation behaviors, including lithium inventory loss, impedance growth, and interfacial instability, which vary significantly across electrode locations and are often masked in conventional bulk analyses. These findings emphasize that electrode-specific aging disparities within pouch cells should not be overlooked in performance assessments and reliability evaluations.

Introduction

The increasing demand for energy and the pressing need for sustainable development have positioned lithium-ion batteries (LIBs) as a foundational technology in energy storage systems. Among various LIB chemistries, $LiFePO_4$//graphite (LFP//Gr) batteries are particularly valued for their intrinsic safety, superior thermal stability, extended cycling durability, and cost-effectiveness, making them well-suited for both electric transportation and large-scale stationary storage. However, despite these favorable attributes, the performance of LFP//Gr batteries inevitably declines during prolonged operation under real-world conditions. This degradation is primarily driven by complex aging mechanisms, including lithium inventory loss, structural fatigue, interfacial side reactions, and the progressive increase in internal resistance,[1–3] all of which compromise capacity retention, reduce power capability, and raise safety

[a]School of Materials Science and Engineering, Beijing Key Laboratory of Environmental Science and Engineering, Beijing Institute of Technology, Beijing 100081, China. E-mail: jydong@bit.edu.cn, suyuefeng@bit.edu.cn, chenlai144@sina.com
[b]Chongqing Innovation Center, Beijing Institute of Technology, Chongqing 401120, China
[c]China Electric Power Research Institute, Beijing 100192, China. E-mail: guanyb@epri.sgcc.com.cn
[d]School of Vehicle and Mobility, Tsinghua University, Beijing 100084, China

and economic concerns. The aging behavior of LFP//Gr batteries thus represents a major constraint for widespread deployment and accurate service life forecasting.[4] In this context, accelerated aging protocols provide a time-efficient approach to emulate long-term degradation behaviors by applying elevated thermal, electrical, or electrochemical stresses. These methodologies facilitate early identification of failure modes and offer valuable insights into stress-dependent degradation kinetics.[4–6] The resulting data are critical for informing material optimization, refining electrode–electrolyte compatibility, and guiding robust battery management strategies.[7,8] Moreover, by correlating accelerated test results with real-world degradation trends, it becomes possible to construct predictive models that enhance reliability and extend functional lifespan.[9] Therefore, in-depth studies of LFP//Gr degradation under accelerated conditions not only contribute to fundamental understanding of failure mechanisms but also support the practical engineering of safer, longer-lasting lithium-ion battery systems for sustainable energy infrastructures.

Temperature serves as a principal driving force in the accelerated aging of lithium-ion batteries, influencing a wide spectrum of physicochemical degradation mechanisms.[10,11] Although substantial progress has been achieved in elucidating thermal effects on overall battery aging, most studies tend to assess the battery as a spatially uniform system, often neglecting potential variations in degradation behavior across different regions of the battery.[12,13] In large-format batteries commonly used in electric vehicles and energy storage systems, such an assumption may be insufficient. Variations in local thermal environments and electrochemical conditions during cycling can introduce region-dependent responses that are not adequately captured by bulk-averaged measurements.[14] In particular, differences between the outer regions and central regions of the battery may arise due to diverse thermal histories, local current distributions, and structural constraints. These spatial distinctions could potentially influence the evolution of degradation phenomena over time.[15,16] However, the extent, origin, and implications of such regional disparities remain poorly understood. Existing diagnostic frameworks rarely account for this intra-battery variability, which may hinder the development of accurate lifetime prediction models and robust design strategies.[17] Therefore, further investigation into the differential aging behaviors between internal and external regions under temperature-accelerated conditions is essential. Such efforts can advance the mechanistic understanding of battery degradation and support the formulation of design and control strategies that are better aligned with the spatial complexity of practical high-capacity batteries.[18,19]

In this study, we investigate the spatial variation in aging behavior of LFP//Gr batteries under different temperature conditions, with particular emphasis on the differences between inner and outer electrode regions during cycling. We selected pouch-type batteries with a rated capacity of 2 Ah and subjected them to temperature-accelerated aging, followed by systematic evaluation of their degradation patterns. To capture the complexity of regional aging phenomena, we employed a multi-scale characterization framework that integrates electrochemical, morphological, and compositional analyses. Rather than relying on spatially averaged data, we focused on resolving region-specific degradation kinetics and failure mechanisms under thermal stress. Our results reveal that elevated temperature not only accelerates overall aging but also amplifies the spatial disparity in degradation behavior, with inner electrode regions exhibiting more severe deterioration than outer regions. Further analysis identifies lithium inventory loss (LLI) as the dominant failure mechanism under high-temperature conditions,[20] primarily driven by continued solid electrolyte interphase (SEI) growth and electrolyte decomposition. These thermally activated side reactions result in irreversible lithium consumption and impedance rise, with varying severity depending on electrode location. The findings highlight the need to consider spatial heterogeneity when evaluating thermal effects on battery aging and provide a mechanistic basis for improving reliability in practical lithium-ion systems.

Results and discussion

To assess the electrochemical degradation behavior of $LiFePO_4$//graphite pouch batteries under different temperature conditions, cycling aging tests were conducted at a constant 1C charge/discharge rate at 25 °C and 45 °C. As illustrated in Fig. 1a, the discharge capacity curves at both temperatures exhibit a two-stage trend. At 25 °C, the battery shows an initial activation period during the first 100 cycles, characterized by a gradual capacity increase. This phenomenon is generally attributed to electrode wetting, electrolyte infiltration, and interfacial stabilization. After this phase, the battery enters a stable linear capacity decline, indicating progressive degradation primarily driven by lithium inventory loss and interfacial deterioration.[21,22] In comparison, the battery cycled at 45 °C does not display a distinct activation stage; instead, it exhibits an early capacity decline due to rapid SEI growth and intensified electrolyte decomposition.[23] Fig. 1b presents the equivalent capacity fade curves, confirming that the degradation rate at 45 °C is consistently faster than at 25 °C. This suggests that elevated temperature accelerates parasitic reactions, leading to earlier onset of irreversible capacity loss. Fig. 1c depicts the corresponding capacity fade rate trends, showing a more pronounced slope for the high-temperature condition, in alignment with the observed degradation behavior. Capacity throughput, defined as the cumulative ampere-hour output over cycles, is presented in Fig. 1d. Batteries cycled at 45 °C deliver higher cumulative capacity in early stages, indicating improved utilization and reaction kinetics under elevated temperature. However, this advantage is progressively offset by enhanced degradation as cycling continues. Fig. 1e shows the evolution of direct current internal resistance (DCIR), revealing higher resistance at 25 °C throughout aging.

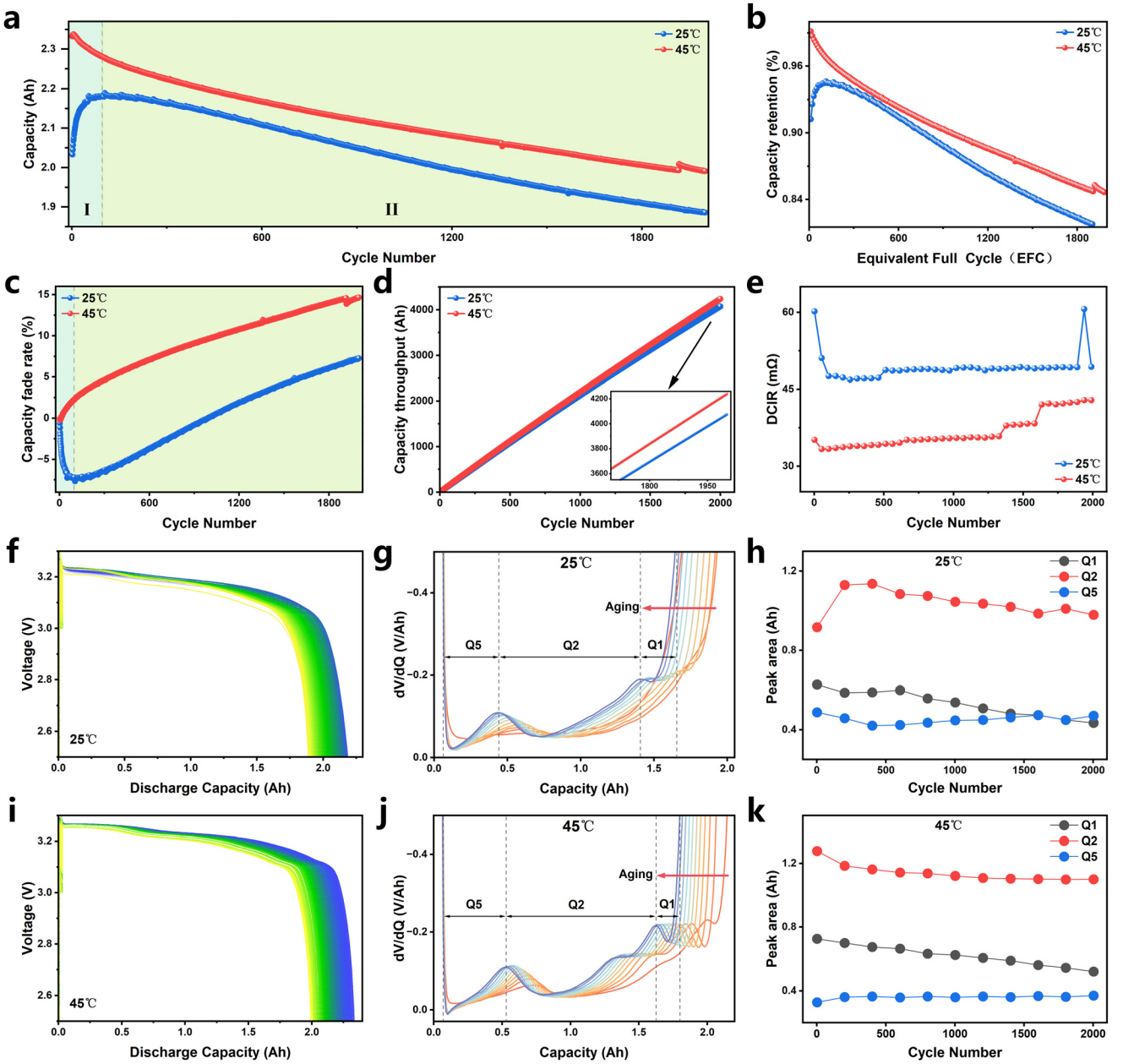

Fig. 1 Comparison of the electrochemical properties of $LiFePO_4$//graphite batteries at 25 °C and 45 °C. (a) Capacity fade curve. (b) Equivalent capacity fade curve. (c) Capacity fade rate. (d) Capacity throughput. (e) DCIR. Discharge curves for (f) at 25 °C and (i) at 45 °C. Differential voltage curves for (g) at 25 °C and (j) at 45 °C. Evolution of peak areas extracted from d*V*/d*Q* curves for (h) at 25 °C and (k) at 45 °C.

This is attributed to decreased ionic mobility, increased electrolyte viscosity, and hindered charge transfer at lower temperature.[24] Conversely, batteries cycled at 45 °C maintain lower DCIR values in the early stage due to enhanced interfacial kinetics and improved mass transport. Together, these findings demonstrate that temperature plays a dual role by simultaneously facilitating early electrochemical activity and accelerating long-term degradation.

The discharge voltage profiles and differential voltage (DV) curves provide further insights into the impact of temperature on the electrochemical aging behavior of $LiFePO_4$//graphite batteries. As shown in Fig. 1f and i, the discharge voltage plateau at 25 °C gradually declines and narrows over prolonged cycling, reflecting the cumulative effects of increased polarization and internal resistance. In contrast, at 45 °C, the voltage plateau exhibits a more rapid decrease and earlier arrival at the cutoff voltage, indicating accelerated degradation of the electrochemical kinetics.[25] This trend is also captured in the DV curves shown in Fig. 1g and j, where a continuous leftward shift and narrowing of the characteristic peaks are observed with increasing cycle number. Such shifts are more pronounced under high-temperature conditions, signifying faster

kinetic decay and declining reversibility of lithium intercalation/deintercalation processes. The peak area evolution, displayed in Fig. 1h and k, further reveals that the Q1 and Q2 regions, associated with Li^+ intercalation at high state-of-charge, progressively decrease with cycling, while Q5 remains relatively unchanged. This selective loss of Q1 capacity highlights that lithium availability during the final stage of charging is notably diminished under thermal stress, likely due to enhanced side reactions such as electrolyte oxidation and SEI overgrowth.[26,27] The accelerated reduction of Q1 under 45 °C conditions confirms that lithium inventory loss (LLI) dominates the aging mechanism, and is further intensified by elevated temperature These findings are consistent with the capacity and impedance results discussed earlier, reinforcing that increased thermal exposure substantially intensifies degradation rates by promoting irreversible side reactions, reducing lithium utilization, and accelerating the decay of electrode kinetics.[28]

Building upon the electrochemical performance analysis, *in situ* electrochemical impedance spectroscopy (EIS) at different voltages was collected to clarify the internal impedance change (Fig. S1). Fresh batteries exhibit low impedance at both 25 °C and 45 °C, indicating favorable interfacial conditions. The slightly higher impedance at 45 °C may be attributed to minor side reactions. In contrast, cycled batteries demonstrate significantly increased impedance at 25 °C and 45 °C, revealing charge transfer limitations and intensified polarization during aging. Notably, the impedance surge is more pronounced at elevated temperatures, signifying that high temperatures accelerate interfacial degradation and side reaction processes. Further insight into the temperature-dependent degradation kinetics was obtained by conducting Distribution of Relaxation Times (DRT) analysis and *in situ* expansion measurements. The DRT technique enables resolution of overlapping impedance contributions by separating resistive elements into characteristic time constants, particularly the charge-transfer resistance (R_{ct}) and the lithium-ion transport resistance at the electrode–electrolyte interface (R_{EEI}).[29] As shown in Fig. 2a and b, the DRT spectra of the pristine battery reveal that the R_{ct}-related peak at 25 °C is considerably higher than that at 45 °C, suggesting that lower temperatures significantly suppress interfacial charge transfer and slow Li^+ mobility due to reduced ionic conductivity and higher electrolyte viscosity. Following prolonged cycling, the batteries aged at 45 °C exhibited substantial increases in both R_{ct} and R_{EEI} peak intensities, as illustrated in Fig. 2c and d, indicating

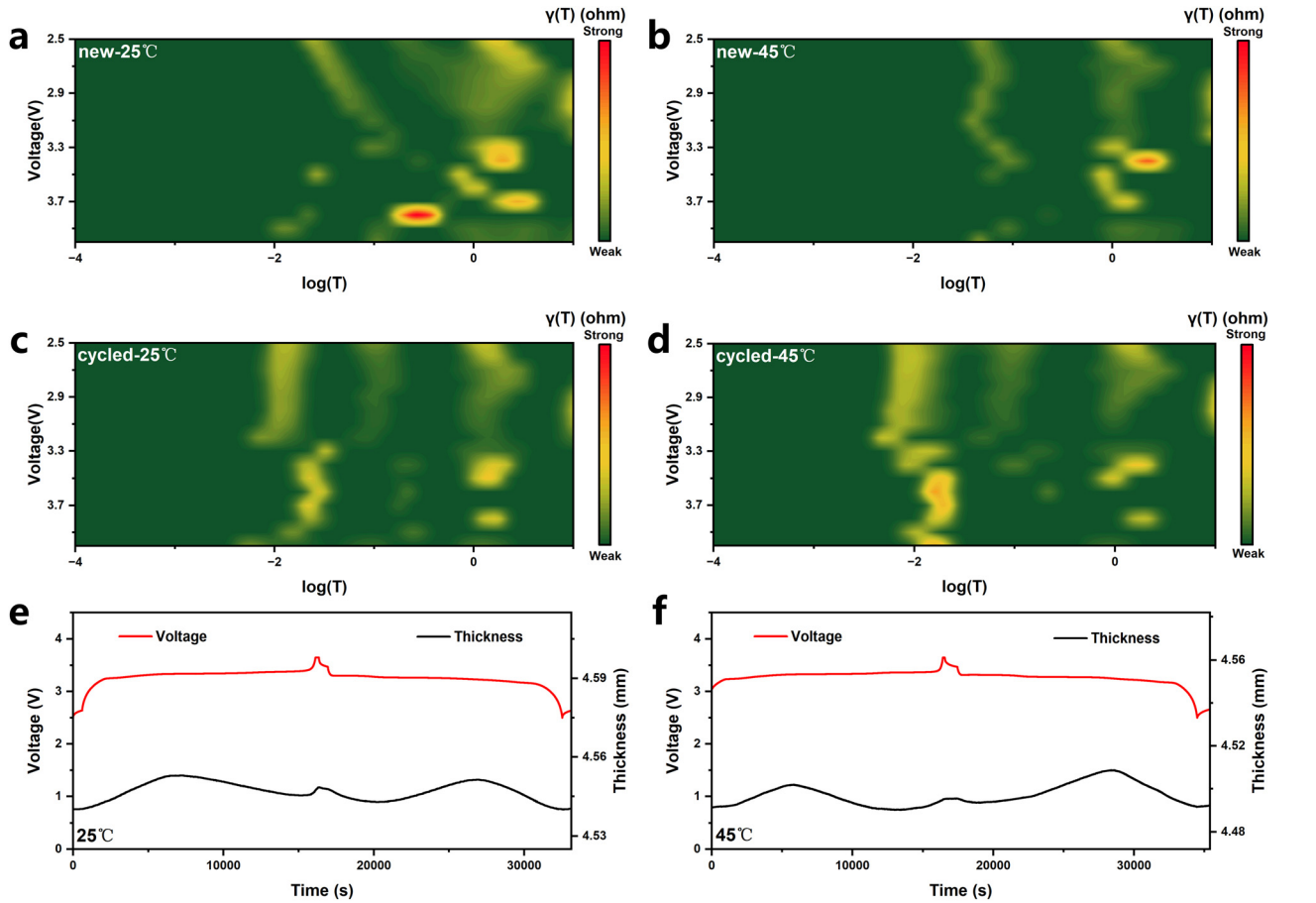

Fig. 2 DRT patterns of fresh batteries (a) at 25 °C and (b) at 45 °C. DRT patterns of cycled batteries (c) at 25 °C and (d) at 45 °C. *In situ* mechanical testing of phase transition and expansion changes: *in situ* expansion analysis for (e) at 25 °C and (f) at 45 °C.

that high-temperature operation intensifies interfacial side reactions and accelerates the degradation of electrochemical kinetics. This behavior is typically associated with the formation and thickening of surface films such as the solid electrolyte interphase (SEI) and cathode electrolyte interphase (CEI), which hinder ion transport and contribute to impedance growth.[30]

In addition to electrochemical characterization, *in situ* expansion monitoring was employed to track thickness evolution during charge/discharge processes. The results reveal that the amplitude of cell expansion is notably greater at 45 °C compared to 25 °C, reflecting more severe mechanical strain during lithium (de)intercalation. Moreover, the thickness-voltage profiles exhibit asymmetrical behavior between charging and discharging phases, indicating irreversible deformation and residual stress accumulation. These mechanical changes can be attributed to temperature-enhanced gas evolution, structural relaxation of polymeric binders, or irreversible particle-level transformations.[31] Together, the aggravated kinetic resistance and mechanical instability under elevated temperature conditions confirm that temperature plays a central role in accelerating battery aging by promoting both electrochemical and physical degradation pathways.

Following the electrochemical and kinetic analyses, morphological and structural characterizations were conducted to further elucidate the microstructural evolution of the cathode under temperature-accelerated aging conditions. Scanning electron microscopy (SEM) and energy-dispersive X-ray spectroscopy (EDS) were employed to examine the cathode surfaces from both fresh and cycled batteries. As presented in Fig. S2, the pristine cathode exhibits a homogeneously distributed elemental profile, indicating a uniform electrode structure prior to cycling. However, after prolonged cycling, the aged cathodes reveal notable spatial variations in morphology and surface composition depending on both temperature and electrode location. SEM images of samples collected from inner and outer regions at 25 °C and 45 °C (Fig. 3a–d) display progressively increasing deposition of surface films and side reaction products with rising temperature, particularly concentrated on the inner region of the 45 °C sample. This observation suggests that elevated temperature exacerbates electrolyte decomposition and gas evolution, leading to more pro-

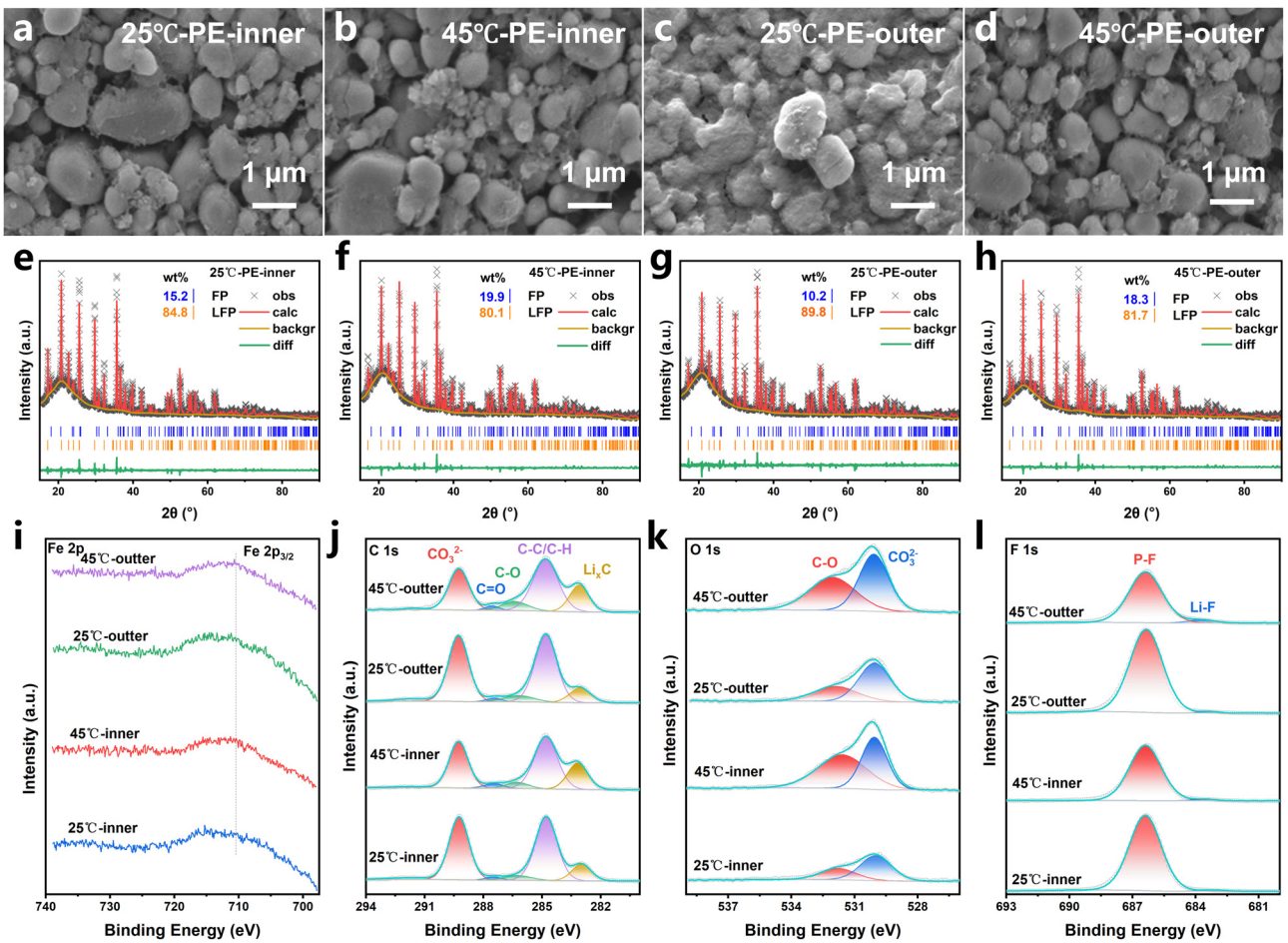

Fig. 3 SEM images of inner cathode (a) at 25 °C and (b) at 45 °C, outer cathode (c) at 25 °C and (d) at 45 °C. XRD Rietveld refinement patterns of inner cathode (e) at 25 °C and (f) at 45 °C, outer cathode (g) at 25 °C and (h) at 45 °C. XPS spectra of (i) Fe 2p, (j) C 1s, (k) O 1s, (l) F 1s for inner and outer cathodes at 25 °C and 45 °C.

nounced surface contamination and passivation, especially within the core electrode areas.[32,33] Complementary EDS mapping of the post-cycling cathodes (Fig. S3–6) further confirms a non-uniform distribution of key elements such as phosphorus, oxygen, and fluorine, implying region-dependent accumulation of degradation products associated with salt decomposition and binder breakdown.[34] To probe the crystallographic evolution, X-ray diffraction (XRD) with Rietveld refinement was performed (Fig. 3e–h). The patterns confirm the coexistence of $LiFePO_4$ (LFP) and its delithiated counterpart $FePO_4$ (FP), with the FP phase reflecting irreversible lithium extraction during cycling. Importantly, quantitative refinement results reveal that the inner electrode regions at 45 °C exhibit significantly higher FP content than those at 25 °C or the outer regions, suggesting enhanced structural degradation and lithium inventory loss in the electrode core.[35] These findings indicate that temperature not only accelerates the degradation process but also intensifies spatial heterogeneity in structural evolution, contributing to uneven capacity fading and mechanical instability across the electrode thickness.

To elucidate the structural and interfacial evolution of the cathode under temperature-accelerated aging, Raman spectroscopy was performed to evaluate the local bonding environment of the active material. As shown in Fig. S7, cathodes from both 25 °C and 45 °C aged cells exhibited consistent Raman signals centered at 996 cm^{-1}, corresponding to the symmetric stretching vibration of the PO_4^{3-} group in $LiFePO_4$. No notable deviations from the spectra of fresh electrodes (Fig. S8) were observed, indicating that the crystal structure of $LiFePO_4$ remains largely unaffected after cycling. As shown in Fig. S9 and 10, the spectra of the $LiFePO_4$ cathode exhibit several characteristic absorption bands. The peaks at 950, 1045, and 1140 cm^{-1} are attributed to the asymmetric stretching vibrations of the PO_4^{3-} group, while the band near 883 cm^{-1} corresponds to the bending vibration of CO_3^{2-}, indicating the formation of surface Li_2CO_3. Additionally, the absorption band at 840 cm^{-1} is assigned to the P–F bond, which likely arises from residual $LiPF_6$ decomposition products.[36] These observations confirm the presence of phosphate- and carbonate-related compounds on the cycled cathode surface. These findings suggest that the positive electrode's bulk structure contributes minimally to the observed capacity decay. To further investigate the chemical evolution of the cathode-electrolyte interphase, XPS analysis was conducted. The Fe $2p_{3/2}$ peaks displayed negligible shifts across all samples (Fig. 3i), suggesting the Fe oxidation state remains stable. However, temperature-induced differences were evident in the surface chemistry. Specifically, the C 1s spectra (Fig. 3j–l) showed a decline in CO_3^{2-}, C═O, C–C/C–H, and $LixC_6$ signals at higher temperatures, indicating consumption of organic species through thermally activated decomposition. Meanwhile, the O 1s spectra revealed an increase in C–O and CO_3^{2-} species at 45 °C, especially in inner electrode regions, implying more severe electrolyte decomposition near the cell core.[37] The F 1s spectra confirmed the presence of LiF, a typical decomposition product of $LiPF_6$, with relatively unchanged intensity across temperatures, whereas P–F signal intensity decreased with temperature, suggesting reduced residual salt content. The P 2p spectra clearly show two major components: the peak at 133.3 eV corresponds to P═O/P–O bonds originating from the $LiFePO_4$ framework (Fig. S11), while the peak at 136.1 eV is attributed to P–F bonds, commonly associated with $LiPF_6$-derived species such as $Li_xPF_yO_z$.[38] As the P═O/P–O component is intrinsic to the cathode, we focused on variations in the P–F signal across different electrode regions. Our results indicate minimal differences in the P–F peak intensity between inner and outer regions, suggesting limited regional variation in $LiPF_6$ decomposition under the studied conditions. These observations highlight that although the active material maintains structural integrity, elevated temperature significantly promotes interfacial degradation processes, particularly through accelerated electrolyte oxidation and surface product accumulation, with inner regions experiencing more pronounced chemical evolution.

To further investigate the spatially dependent degradation phenomena in graphite electrodes under temperature-accelerated aging, SEM and EDS analyses were conducted on samples extracted from both the inner and outer regions of batteries cycled at 25 °C and 45 °C. As shown in Fig. 4a–d, the outer anode surfaces exhibit relatively intact morphology with distinct graphite particle boundaries and minimal observable surface films, irrespective of cycling temperature. In contrast, the inner region of the anode aged at 25 °C displays clear deposit accumulation (Fig. 4a), which becomes substantially more pronounced at 45 °C (Fig. 4b). The significant increase in surface coverage and morphological roughness with rising temperature suggests enhanced interfacial reactions between the electrode and electrolyte, particularly concentrated in the inner core.[39] Complementary EDS mapping (Fig. S12–16) reveals that the pristine anode initially exhibits a spatially uniform elemental distribution with negligible oxygen and fluorine content. However, after cycling, both O and F signals increase notably, with a more prominent enrichment in the inner regions at elevated temperature. This result indicates that temperature elevation accelerates electrolyte decomposition and promotes the growth of thick and spatially heterogeneous SEI layers, which may intensify local transport limitations and electrode polarization.[40,41] These interfacial variations coincide with the morphological evolution observed in SEM images and reflect stronger side reactions under high-temperature cycling conditions. To further assess whether such temperature-driven differences in interfacial degradation influence the structural stability of the graphite framework, X-ray diffraction was performed on electrodes from different regions. As illustrated in Fig. 4e, f and Fig. S17, all aged anode samples display consistent diffraction patterns, including the (002) peak of graphite and signals from the copper current collector. No significant shift in peak position or broadening was observed, indicating that the graphite crystal structure remains largely unchanged after cycling at both temperatures.[42]

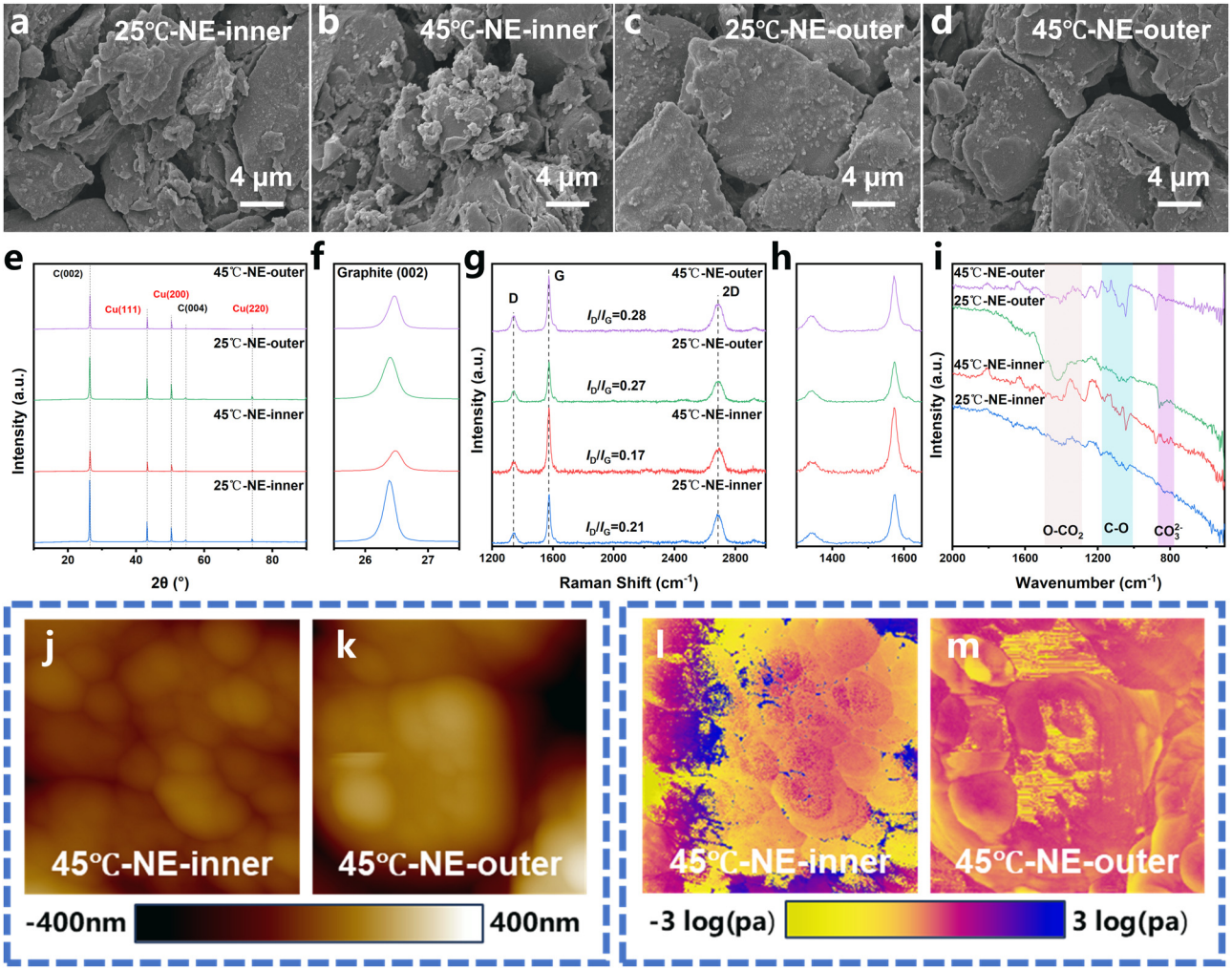

Fig. 4 SEM images of inner anode (a) at 25 °C and (b) at 45 °C, outer anode (c) at 25 °C and (d) at 45 °C. (e and f) XRD patterns of inner and outer anode at 25 °C and 45 °C. (g and h) Raman spectra of inner and outer anode at 25 °C and 45 °C. (i) FTIR spectroscopy of inner and outer anode at 25 °C and 45 °C. AFM analysis of 2D height images for (j) inner anode and (k) outer anode. 2D Young's modulus for (l) inner anode and (m) outer anode.

Building upon the prior characterization of graphite anode morphology and crystal structure, further investigations were conducted to clarify the chemical and mechanical evolution of the anode materials under elevated temperature conditions. Raman spectroscopy was employed to evaluate the structural integrity of the graphite, where a notable increase in the D-to-G band intensity ratio was observed for the anodes aged at 45 °C compared to those at 25 °C (Fig. 4g, h and Fig. S18), indicating a higher concentration of structural defects and more pronounced graphitic disorder.[43] This effect was especially evident in the inner electrode region, implying that increased temperature accelerates localized degradation. Fourier-transform infrared spectroscopy (Fig. 4i and Fig. S19) provided complementary evidence by detecting more prominent absorption peaks at 1122 cm^{-1} and 875 cm^{-1} in the 45 °C-aged samples. These peaks correspond to C–O stretching vibrations and carbonate species, suggesting the accumulation of surface byproducts such as lithium alkyl carbonates and lithium carbonate due to intensified electrolyte decomposition.[44] In contrast, the electrodes aged at 25 °C exhibited weaker absorption signals, reflecting a more stable interfacial environment. To further evaluate the spatial variation of aging phenomena, atomic force microscopy (AFM) was applied to analyze surface morphology and mechanical properties of anode samples from different regions. The topographic maps in Fig. 4j and k show that the inner region displayed significantly rougher surfaces and denser particle-like features compared to the outer region, indicative of thicker and more uneven SEI formation. The corresponding height distribution histogram (Fig. S20) confirmed a wider range of surface roughness in the inner anode. Furthermore, AFM-based modulus mapping (Fig. 4l and m) revealed a broader distribution of Young's modulus values across the inner surface, with a prevalence of lower-modulus domains, indicating reduced mechanical robustness and increased SEI fragility. These results collectively demonstrate that temperature-induced aging not only

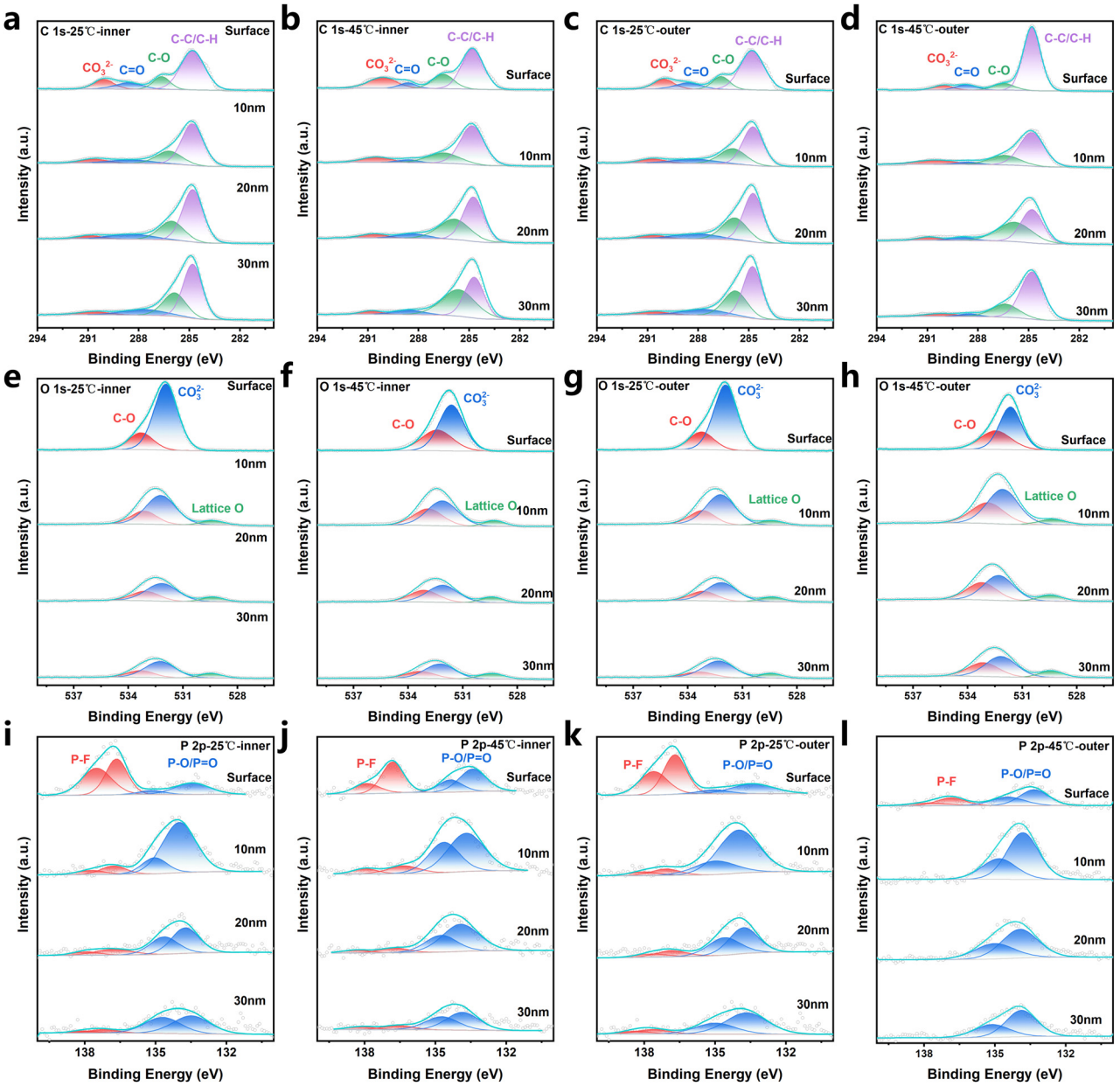

Fig. 5 XPS depth profiles of inner and outer anodes at 25 °C and 45 °C: (a–d) C 1s, (e–h) O 1s, and (i–l) P 2p.

promotes interfacial side reactions but also leads to spatially heterogeneous degradation in both surface composition and mechanical properties of graphite electrodes.[45]

Building upon the morphological and spectroscopic analysis of graphite anodes under different temperature conditions, depth-resolved X-ray photoelectron spectroscopy (XPS) was employed to further investigate the spatial heterogeneity in solid-electrolyte interphase (SEI) evolution. Argon ion etching was conducted at successive depths (0, 10, 20, and 30 nm) to probe the chemical state distribution across both inner and outer regions of the cycled anodes (Fig. 5). The O 1s spectra revealed that SEI layers formed at both 25 °C and 45 °C primarily consisted of C–O and CO_3^{2-} species, but the relative content of C–O bonds was significantly higher in the 45 °C samples, particularly in the inner anode region, indicating enhanced organic SEI accumulation and more pronounced electrolyte decomposition under elevated temperature.[46] Further analysis of the P 2p spectra showed increased signals of P–O and P═O bonds at higher temperatures, especially within the deeper SEI layers of the inner region, suggesting intensified formation of $Li_xPF_yO_z$ species as a result of $LiPF_6$ degradation.[47] These phosphate-containing compounds, associated with salt breakdown, were more abundant and spatially non-uniform in the high-temperature aged samples, confirming that thermal effects not only accelerate the degradation kinetics but also amplify regional disparities in inter-

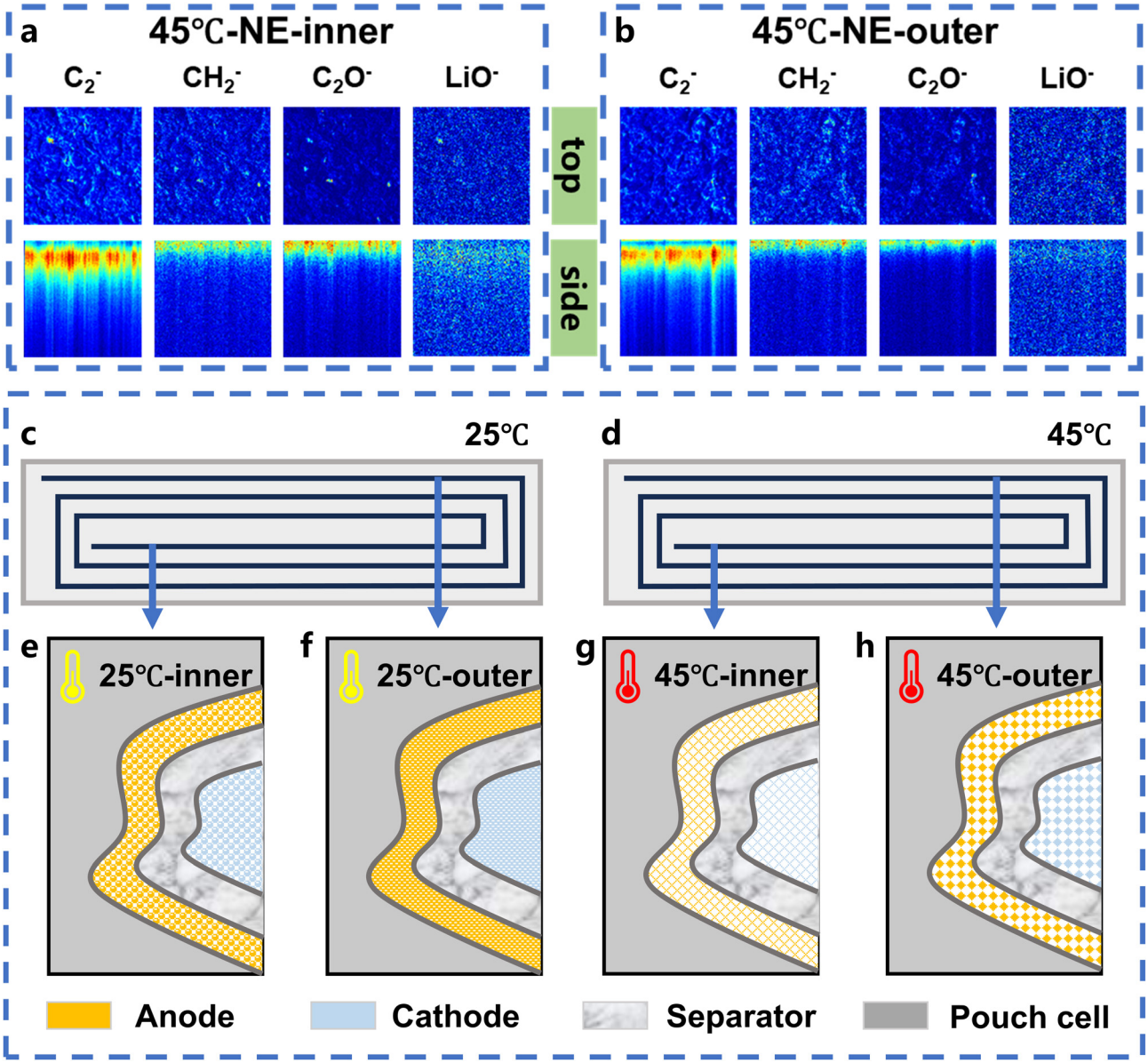

Fig. 6 TOF-SIMS chemical maps of various secondary ion fragments at 45 °C: (a) inner anode and (b) outer anode. Cross-sectional schematic of a pouch cell (c) at 25 °C and (d) 45 °C. (e–h) Schematic diagram of inner and outer cell structure at 25 °C and 45 °C.

facial chemistry. The evident compositional contrast between inner and outer electrode surfaces points to localized degradation mechanisms driven by differences in thermal exposure, electrolyte accessibility, and transport limitations. Together, these findings provide direct evidence that temperature-induced aging in graphite anodes leads to significant spatial heterogeneity in SEI structure and composition, which is closely linked to asymmetric interfacial reactivity and uneven electrochemical performance in lithium-ion batteries.

Building upon the preceding morphological and chemical analyses, the spatial heterogeneity observed in the graphite anode under temperature-accelerated aging conditions was identified as a core contributor to battery degradation. In particular, the significant disparity in surface composition and interfacial reactivity between the inner and outer regions of the graphite electrode emphasizes the critical role of localized failure in determining overall aging behavior. To further elucidate the chemical evolution of the anode surface after high-temperature cycling, time-of-flight secondary ion mass spectrometry (ToF-SIMS) was conducted on the 45 °C aged graphite anode to assess spatial variations in surface composition (Fig. 6). The resulting spectra revealed markedly stronger signals of representative degradation fragments including C_2^-, CH_2^-, C_2O^-, and LiO^- on the inner surface relative to the outer. Specifically, C_2^- and CH_2^- are typically associated with organic species derived from solvent decomposition, such as alkyl carbonates and polymerized byproducts. C_2O^- reflects the presence of oxidized organics including lithium alkyl car-

bonates and partially decomposed electrolyte solvents. LiO^- corresponds to inorganic components such as lithium oxide or hydroxide, typically formed *via* $LiPF_6$ hydrolysis or decomposition. These results provide direct evidence of intensified side reactions and SEI formation in the inner anode region, confirming that elevated temperature not only accelerates interfacial degradation but also promotes significant heterogeneity in aging behavior.[48,49]

Based on the above analysis, temperature-accelerated aging profoundly affects both the overall degradation kinetics and the spatial distribution of failure within $LiFePO_4$//graphite batteries. Elevated temperatures intensify lithium inventory loss through enhanced interfacial side reactions, while also inducing marked spatial disparities in degradation severity between inner and outer electrode regions. Notably, the inner graphite anode experiences more severe aging, characterized by thicker interphase layers, higher accumulation of decomposition products, and increased structural disorder. Similar spatial differentiation is also evident in the cathode, with more pronounced irreversible phase changes and surface deposits occurring closer to the core. These observations confirm that aging is intrinsically non-uniform and that such heterogeneity plays a dominant role in determining long-term battery performance. Meanwhile, the findings from our spatial diagnostic framework may also be applicable to other battery systems, particularly high-Ni layered oxide cathodes and sodium-ion batteries. In high-Ni systems, spatially heterogeneous degradation is frequently associated with lithium concentration gradients, mechanical stress accumulation, and uneven CEI formation during cycling, especially under high-voltage and high-temperature conditions.[50] Similarly, sodium-ion batteries also face challenges related to structural instability and region-dependent degradation due to differences in ionic radius and transport behavior.[51] Therefore, the spatially resolved methodology presented in this work may serve as a useful tool for revealing localized aging behaviors and guiding design optimization in both lithium- and sodium-based energy storage systems. The recognition of spatially resolved degradation under temperature stress provides crucial insight into failure mechanisms and highlights the importance of incorporating spatial heterogeneity considerations into battery design, modeling, and reliability assessment frameworks.[52]

Conclusions

This study systematically elucidates the temperature-dependent spatial heterogeneity in the aging behavior of $LiFePO_4$// graphite pouch batteries through integrated multi-scale analysis. Under accelerated cycling conditions, batteries operated at 45 °C exhibit significantly faster degradation than those cycled at 25 °C, with more pronounced regional disparities observed between inner and outer electrode areas. The inner regions are subject to more severe capacity loss, impedance rise, and interfacial deterioration, indicating a localized intensification of degradation mechanisms. The primary cause of performance decline is identified as lithium inventory loss, which results from sustained side reactions and progressive instability at the electrode–electrolyte interface. These outcomes demonstrate that battery aging cannot be sufficiently understood through homogeneous assumptions alone. Instead, spatial heterogeneity plays a decisive role in determining the progression and severity of failure modes. The multi-scale insights provided in this work offer a mechanistic foundation for spatially adaptive design strategies, improved thermal regulation, and more accurate lifetime prediction models, thereby supporting the advancement of durable and reliable lithium-ion energy storage systems in demanding application environments.

Author contributions

Jialong Zhou: writing-original draft, methodology, data curation, conceptualization. Jinyang Dong: writing – visualization, software, methodology. Yun Lu: methodology, investigation. Kang Yan: methodology, investigation. Yibiao Guan: methodology, investigation. Fangzi Zhao: methodology, investigation. Rui Tang: methodology, investigation. Wenjun Shen: methodology, investigation. Ning Li: methodology, investigation. Yuefeng Su: writing-review & editing, supervision, resources, project administration. Feng Wu: resources, funding acquisition, conceptualization. Lai Chen: writing-review & editing, supervision, resources, project administration.

Conflicts of interest

There are no conflicts to declare.

Data availability

The DRT analysis software used in this study was developed by the research group of Francesco Ciucci, and is available for download at [**https://github.com/ciuccislab**]. The software for Gsas1 can be found at [**https://subversion.xray.aps.anl.gov/trac/EXPGUI**].

Electronic supplementary information (ESI) available. See DOI: **https://doi.org/10.1039/d5eb00131e**.

Acknowledgements

This work was supported by the National Key R&D Program of China (2021YFB2401800). L. Chen acknowledges the support from Beijing Nova Program (20230484241). J. Y. Dong acknowledges the support from the China Postdoctoral Science Foundation (2024M754084) and the Postdoctoral Fellowship Program of CPSF (GZB20230931). The authors also thank for the support from Initial Energy Science & Technology Co., Ltd (IEST).

References

1 Y. Peng, M. Ding, K. Zhang, H. Zhang, Y. Hu, Y. Lin, W. Hu, Y. Liao, S. Tang, J. Liang, Y. Wei, Z. Gong, Y. Jin and Y. Yang, *ACS Energy Lett.*, 2024, **9**, 6022–6028.
2 S. Li and R. J. E. B. Yazami, *EES Batteries*, 2025, **1**, 808–812.
3 Y. Liao, H. Zhang, Y. Peng, Y. Hu, J. Liang, Z. Gong, Y. Wei and Y. Yang, *Adv. Energy Mater.*, 2024, **14**, 2304295.
4 Y. Lin, W. Hu, M. Ding, Y. Hu, Y. Peng, J. Liang, Y. Wei, A. Fu, J. Lin and Y. Yang, *Adv. Energy Mater.*, 2024, **14**, 2400894.
5 R. Li, L. Bao, L. Chen, C. Zha, J. Dong, N. Qi, R. Tang, Y. Lu, M. Wang and R. J. S. B. Huang, *Sci. Bull.*, 2023, **68**, 3055–3079.
6 J.-L. Li, Y.-N. Wang, S.-Y. Sun, Z. Zheng, Y. Gao, P. Shi, Y.-J. Zhao, X. Li, Q. Li, X.-Q. Zhang and J.-Q. Huang, *Adv. Energy Mater.*, 2025, **15**, 2403845.
7 S. Tao, M. Zhang, Z. Zhao, H. Li, R. Ma, Y. Che, X. Sun, L. Su, C. Sun, X. Chen, H. Chang, S. Zhou, Z. Li, H. Lin, Y. Liu, W. Yu, Z. Xu, H. Hao, S. Moura, X. Zhang, Y. Li, X. Hu and G. Zhou, *Energy Environ. Sci.*, 2025, **18**, 1544–1559.
8 Z. Zheng, X. Liu, X.-Q. Zhang, S.-Y. Sun, J.-L. Li, Y.-N. Wang, N. Yao, D.-H. Zhan, W.-J. Feng, H.-J. Peng, J.-K. Hu, J.-Q. Huang and Q. Zhang, *Angew. Chem., Int. Ed.*, 2025, **64**, e202507387.
9 S. Tang, Y. Liang, Y. Peng, Y. Hu, Y. Liao, X. Yang, H. Zhang, Y. Lin, K. Zhang, J. Liang, B. Li, G. Zhao, Y. Wei, Z. Gong and Y. Yang, *Adv. Energy Mater.*, 2025, **15**, 2402842.
10 P. Ombrini, Q. Wang, A. Vasileiadis, F. Wu, Z. Gao, X. Hu, M. van Hulzen, B. Li, C. Zhao and M. J. E. B. Wagemaker, *EES Batteries*, 2025, **1**, 437–449.
11 H. Zhang, Y. Peng, Y. Hu, S. Pan, S. Tang, Y. Luo, Y. Liang, Y. Liao, Y. Lin, K. Zhang, Y. Wei, J. Liang, Y. Jin and Y. Yang, *Adv. Energy Mater.*, 2025, **15**, 2404997.
12 S. Li, H. Zhang, Y. Liu, L. Wang and X. He, *Adv. Funct. Mater.*, 2024, **34**, 2310057.
13 Y. Peng, C. Zhong, M. Ding, H. Zhang, Y. Jin, Y. Hu, Y. Liao, L. Yang, S. Wang, X. Yin, J. Liang, Y. Wei, J. Chen, J. Yan, X. Wang, Z. Gong and Y. Yang, *Adv. Funct. Mater.*, 2024, **34**, 2404495.
14 R. Tang, J. Dong, C. Wang, Y. Guan, A. Yin, K. Yan, Y. Lu, N. Li, G. Zhao, B. Li, W. Shen, F. Wu, Y. Su and L. Chen, *Adv. Funct. Mater.*, 2025, **35**, 2421284.
15 Y. Cao, J. Li, D. Tang, F. Zhou, M. Yuan, Y. Zhu, C. Feng, R. Shi, X. Wei, B. Wang, Y. Song, H.-M. Cheng and G. Zhou, *Adv. Mater.*, 2024, **36**, 2414048.
16 K. Jia, J. Ma, J. Wang, Z. Liang, G. Ji, Z. Piao, R. Gao, Y. Zhu, Z. Zhuang, G. Zhou and H.-M. Cheng, *Adv. Mater.*, 2023, **35**, 2208034.
17 J. Li, R. Shi, J. Wang, Y. Cao, H. Ji, J. Tang, G. Ji, W. Chen, M. Zhang, X. Xiao and G. Zhou, *Adv. Mater.*, 2025, **37**, 2414235.
18 D. Tang, G. Ji, J. Wang, Z. Liang, W. Chen, H. Ji, J. Ma, S. Liu, Z. Zhuang and G. Zhou, *Adv. Mater.*, 2024, **36**, 2309722.
19 X.-X. Zhao, X.-T. Wang, J.-Z. Guo, Z.-Y. Gu, J.-M. Cao, J.-L. Yang, F.-Q. Lu, J.-P. Zhang and X.-L. Wu, *Adv. Mater.*, 2024, **36**, 2308927.
20 Z. Li, Y.-X. Yao, M. Zheng, S. Sun, Y. Yang, Y. Xiao, L. Xu, C.-B. Jin, X.-Y. Yue, T. Song, P. Wu, C. Yan and Q. Zhang, *Angew. Chem.*, 2025, **137**, e202409409.
21 C. Feng, Y. Cao, L. Song, B. Zhao, Q. Yang, Y. Zhang, X. Wei, G. Zhou and Y. Song, *Angew. Chem., Int. Ed.*, 2025, **64**, e202418198.
22 X. Jia, H. Kang, G. Hou, W. Wu, S. Lu, Y. Li, Q. Wang, W. Qin and X. Wu, *Angew. Chem., Int. Ed.*, 2024, **63**, e202318248.
23 D. Yang, Z. Fang, Y. Ji, Y. Yang, J. Hou, Z. Zhang, W. Du, X. Qi, Z. Zhu, R. Zhang, P. Hu, L. Qie and Y. Huang, *Angew. Chem., Int. Ed.*, 2024, **63**, e202409929.
24 X. Bai, Y. Sun, X. Li, R. He, Z. Liu, J. Pan and J. Zhang, *Electrochem. Energy Rev.*, 2024, **7**, 33.
25 Y. Ding, Z. P. Cano, A. Yu, J. Lu and Z. Chen, *Electrochem. Energy Rev.*, 2019, **2**, 1–28.
26 H. Gao, N. S. Grundish, Y. Zhao, A. Zhou and J. B. Goodenough, *Energy Mater. Adv.*, 2021, **2021**, 1932952.
27 W. Mei, L. Jiang, C. Liang, J. Sun and Q. Wang, *Energy Storage Mater.*, 2021, **41**, 209–221.
28 R. Xiong, Y. Sun, C. Wang, J. Tian, X. Chen, H. Li and Q. Zhang, *Energy Storage Mater.*, 2023, **57**, 460–470.
29 M. Xu, C. Wu, F. Zhang, Y. Zhang, J. Ren, C. Zhang, X. Wang, L. Xiao, O. Fontaine and J. Qian, *Energy Storage Mater.*, 2024, **71**, 103611.
30 Z. Zeng, H. Lei, X. Lu, C. Zhu, Y. Wen, J. Zhu, X. Ji, W. Sun, Y. Yang and P. Ge, *Energy Storage Mater.*, 2025, **74**, 103947.
31 L. Wang, J. Qiu, X. Wang, L. Chen, G. Cao, J. Wang, H. Zhang and X. He, *eScience*, 2022, **2**, 125–137.
32 X. Han, L. Lu, Y. Zheng, X. Feng, Z. Li, J. Li and M. Ouyang, *eTransportation*, 2019, **1**, 100005.
33 Y. Huang, *Interdiscip. Mater.*, 2022, **1**, 323–329.
34 X. Feng, D. Ren, X. He and M. Ouyang, *Joule*, 2020, **4**, 743–770.
35 Y. Jin, Z. Zheng, D. Wei, X. Jiang, H. Lu, L. Sun, F. Tao, D. Guo, Y. Liu, J. Gao and Y. Cui, *Joule*, 2020, **4**, 1714–1729.
36 Y. Jia, X. Gao, L. Ma and J. Xu, *Adv. Energy Mater.*, 2023, **13**, 2300368.
37 R. Malik, *Joule*, 2018, **2**, 2204–2205.
38 A. Geslin, L. Xu, D. Ganapathi, K. Moy, W. C. Chueh and S. Onori, *Nat. Energy*, 2025, **10**, 172–180.
39 P. Xu, Q. Dai, H. Gao, H. Liu, M. Zhang, M. Li, Y. Chen, K. An, Y. S. Meng, P. Liu, Y. Li, J. S. Spangenberger, L. Gaines, J. Lu and Z. Chen, *Joule*, 2020, **4**, 2609–2626.
40 Z. Sun, J. Yang, H. Xu, C. Jiang, Y. Niu, X. Lian, Y. Liu, R. Su, D. Liu, Y. Long, M. Wang, J. Mao, H. Yang, B. Cui, Y. Xiao, G. Chen, Q. Zhang, Z. Xing, J. Pan, G. Wu and W. Chen, *Nano-Micro Lett.*, 2024, **16**, 141.
41 S. Chen, G. Wu, H. Jiang, J. Wang, T. Chen, C. Han, W. Wang, R. Yang, J. Zhao, Z. Tang, X. Gong, C. Li, M. Zhu, K. Zhang, Y. Xu, Y. Wang, Z. Hu, P. Chen, B. Wang, K. Zhang, Y. Xia, H. Peng and Y. Gao, *Nature*, 2025, **638**, 676–683.

42 H. Zhao, H. D. Deng, A. E. Cohen, J. Lim, Y. Li, D. Fraggedakis, B. Jiang, B. D. Storey, W. C. Chueh, R. D. Braatz and M. Z. Bazant, *Nature*, 2023, **621**, 289–294.
43 J. Dong, Y. Xue, C. Zhang, Q. Weng, P. Dai, Y. Yang, M. Zhou, C. Li, Q. Cui and X. J. A. M. Kang, *Adv. Mater.*, 2017, **29**, 1603692.
44 X.-G. Yang, T. Liu and C.-Y. Wang, *Nat. Energy*, 2021, **6**, 176–185.
45 A. Adamson, K. Tuul, T. Botticher, S. Azam, M. D. L. Garayt and M. Metzger, *Nat. Mater.*, 2023, **22**, 1380–1386.
46 H. D. Deng, H. Zhao, N. Jin, L. Hughes, B. H. Savitzky, C. Ophus, D. Fraggedakis, A. Borbély, Y.-S. Yu, E. G. Lomeli, R. Yan, J. Liu, D. A. Shapiro, W. Cai, M. Z. Bazant, A. M. Minor and W. C. Chueh, *Nat. Mater.*, 2022, **21**, 547–554.
47 W. Bao, W. Yao, Y. Li, B. Sayahpour, B. Han, G. Raghavendran, R. Shimizu, A. Cronk, M. Zhang, W. Li and Y. S. Meng, *Energy Environ. Sci.*, 2024, **17**, 4263–4272.
48 W. Shi, L. Liu, R. Xu, R. Sun, J. Dong and X. Kang, *Energy Storage Mater.*, 2025, **76**, 104143.
49 S. Solchenbach, C. Tacconis, A. Gomez Martin, V. Peters, L. Wallisch, A. Stanke, J. Hofer, D. Renz, B. Lewerich, G. Bauer, M. Wichmann, D. Goldbach, A. Adam, M. Spielbauer, P. Lamp and J. Wandt, *Energy Environ. Sci.*, 2024, **17**, 7294–7317.
50 Y. Liu, Q. Wang, L. Chen, Z. Xiao, X. Fan, S. Ma, L. Ming, A. Tayal, B. Zhang, F. Wu and X. Ou, *Mater. Today*, 2022, **61**, 40–53.
51 M. Zhang, S. Wang, J. Zhu, F. Zheng, Y. Jiang, S. Hu, Y. Li, Y. Huang, Q. Pan, H. Wang, X. Ou and Q. Li, *Adv. Funct. Mater.*, 2025, **35**, 2500165.
52 D. Meng, Z. Xue, G. Chen, D. Zhou, Y.-S. He, Z.-F. Ma, Y. Liu and L. Li, *Energy Environ. Sci.*, 2024, **17**, 4658–4669.